Kinematic characteristics and water mass transports of submesoscale coherent vortices in the northeastern South China Sea

Yi Wei[1,2,3], Zhiwei Zhang[1,2], Xincheng Zhang[1,4*], Zhongbin Sun[1,4], Wei Zhao[1,2], Jiwei Tian[1,2]

[1]Frontier Science Center for Deep Ocean Multispheres and Earth System (FDOMES) and Physical Oceanography Laboratory/Key Laboratory of Ocean Observation and Information of Hainan Province, Sanya Oceanographic Institution, Ocean University of China, Qingdao/Sanya, China.

[2]Laoshan Laboratory, Qingdao, China.

[3]Academy of the Future Ocean, Ocean University of China, Qingdao, China.

[4]College of Oceanic and Atmospheric Sciences, Ocean University of China, Qingdao, China.

[*] Correspondence to: Xincheng Zhang, zhangxincheng@ouc.edu.cn

Key points

1. Dozens of submesoscale coherent vortices (SCVs) are observed at moorings in the northeastern South China Sea based on a mooring array
2. The kinematic characteristics of the SCVs are statistically analyzed
3. Water mass transports induced by the SCVs are quantified

Abstract

As a unique phenomenon occurring in the subsurface ocean, submesoscale coherent vortices (SCVs) are believed to have a pivotal role in the long-distance ocean tracer transports. SCVs have been widely observed in the global oceans, however, most of them are captured accidentally and their kinematic characteristics and water mass transports have only been studied in a limited number of regions. Here, we use 4-year observations of velocity, temperature, and salinity from five moorings in the northeastern South China Sea (NESCS) to examine dozens of newly discovered SCVs. A total of 34 SCVs were identified during the observational period, including 25 convex lens-like anticyclones and 9 concave lens-like cyclones. The maximum swirl velocity, mean radius, and vertical length scale of the anticyclones (cyclones) are 0.19±0.07 m s^{-1} (0.19±0.07 m s^{-1}), 26.4±13.9 km (17.0±5.4 km), and 204±62 m (188±53 m), respectively. Vertically, the velocity structure of the observed SCVs conforms to a Gaussian function when the effect of stratification is removed. Water mass analyses suggest that 88% (30/34) of the SCVs carried Kuroshio water, which demonstrates the mechanism proposed by Zhang et al. (2022) that they are formed by Kuroshio-islands interactions within the Luzon Strait. This category of SCVs is therefore named Luzon Strait island wake eddies (Liddies). We further estimate that Liddies can result in an equivalent annual-mean volume transport of 0.20 Sv westward across the Luzon Strait, which suggests that they play a nonnegligible role in the subsurface water transports between the NESCS and the northwestern Pacific.

Plain Language Summary

Submesoscale coherent vortices (SCVs) are unique anticyclonic or cyclonic eddies which occur in subsurface oceans. SCVs have the capability to transport water for long distances, and therefore, they may play a significant part in tracer transports of the subsurface ocean. Nevertheless, because of the paucity of long-term in situ SCV observations, their statistical kinematic characteristics and water mass transports are still poorly quantified. Here, based on 4-year velocity and temperature/salinity measurements of five moorings in the northeastern South China Sea (NESCS), 34 SCVs are identified, 9 of which are cyclones, and the rest are anticyclones, and their statistical kinematic characteristics (e.g., maximum swirl velocity, radius, and vertical length scale, etc.) are revealed. The swirl velocity structures of SCVs in vertical share a uniform Gaussian. We also find that ~90% of the observed SCVs contained water from the Kuroshio current, demonstrating the mechanism of Kuroshio-islands interactions in the Luzon Strait which generate SCVs. These SCVs can lead to significant westward volume transport through the Luzon Strait into the NESCS, suggesting that SCVs play a nonnegligible role in NESCS-northwestern Pacific subsurface water exchange and thus have potential impacts on marine ecosystems and biogeochemical cycles.

1. Introduction

The upper mixed layer of the ocean is abundant with submesoscale processes that have spatial scales of O(1–10) km and temporal scales of O(1–10) days with O(1) Rossby and Burger numbers (McWilliams, 2016; Taylor and Thompson, 2023). In addition to those in the upper mixed layer, a unique submesoscale phenomenon called submesoscale coherent vortices (SCVs) can occur within or beneath the thermocline (McWilliams, 1985). SCVs typically have much longer lifespans (sometimes up to years) than the upper-layer submesoscale processes due to the absence of external forcing and thus weak dissipation in the ocean interior. As a result, SCVs can transport source water hundreds to thousands of kilometers away from their origins, which is likely to have a significant impact on subsurface tracer transports (Bosse et al., 2017; Bower et al., 2013; Collins et al., 2013; Frenger et al., 2018; Li et al., 2017; Pelland et al., 2013; Richardson et al., 1989; Zhang et al., 2015).

In order to provide readers with a more intuitive understanding of SCVs, we show the composite three-dimensional structures of SCVs identified in the northeastern South China Sea (NESCS) in Figure 1. As we can see, SCVs have weak expressions at the sea surface and their horizontal scales are smaller than the first baroclinic Rossby deformation radius. This makes them difficult to be investigated by traditional satellite and in situ observations as applied to surface-intensified mesoscale eddies (Adams et al., 2017; Zhang et al., 2016, 2021). Till to now, most of the reported SCVs were discovered by accident from shipboard profiles of Conductivity-Temperature-Depth (CTD) and Acoustic Doppler Current Profiler

(ADCP), moorings, and subsurface floats. In addition, SCVs have only been systematically studied in a few certain regions, for instance, the Mediterranean Water eddies (Meddies) of North Atlantic (Bashmachnikov et al., 2015; Bower et al., 1997; McDowell & Rossby, 1978; Richardson et al., 1991), the California Undercurrent eddies (Cuddies) of northeastern Pacific (Collins et al., 2013; Garfield et al., 1999; Pelland et al., 2013; Steinberg et al., 2019; Torres et al., 2017), and the Kuroshio Extension region intermediate-layer eddies (Kiddies) of northwestern Pacific (NWP; Li et al., 2017; Zhang et al., 2015; Zhu et al., 2021). The ever-increasing utilization of Argo float profiles has further revealed that SCVs widely exist in the world ocean (McCoy et al., 2020). However, statistically robust kinematic characteristics and water mass transports of SCVs on the global scope remain unknown (Gula et al., 2021).

The South China Sea (SCS) is abundant with energetic multiscale dynamic processes due to complex forcing factors such as a strong Asian monsoon, complicated topography, and Kuroshio intrusions (see Sun et al., 2022 and references therein). Basin-scale circulation, mesoscale eddies, small-scale internal waves, and microscale turbulent mixing in the SCS have all been extensively studied, but it is only recently that submesoscale processes have been explored thanks to improved resolution of in situ observations and numerical simulations (e.g., Cao et al., 2019; Dong et al., 2022; Dong and Zhong, 2018; Lin et al., 2020; Song et al., 2022; Zhang et al., 2016, 2020; Zhong et al., 2017). However, most previous efforts only considered submesoscale processes in the upper mixed layer, and the knowledge of

SCVs in the SCS is still lacking.

Based on observations of concurrent velocity, temperature, and salinity data from a high-resolution mooring array in the NESCS, the recent research in Zhang et al. (2022) discovered a pair of opposite-polarity SCVs for the first time. One of these SCVs had trapped Kuroshio water, and it was proposed that it was formed by Kuroshio-islands interactions within the Luzon Strait. In addition, it was also suggested that when a SCV migrates across a mooring site, it can be properly identified using time series data from moored velocity and temperature/salinity (T/S) profiles. We here further expand on Zhang et al. (2022) by conducting broader investigations of the kinematic characteristics and water mass transports of SCVs in the NESCS, with the help of 4-year-long observations from a mesoscale-resolving mooring array west of the Luzon Strait (Sun et al., 2020, 2022). The remaining part of this paper proceeds as follows. Section 2 introduces the data and methods. Section 3 presents the kinematic characteristics of SCVs containing a description of two SCV cases, the SCVs' vertical structure, and statistical characteristics of SCVs' kinematic parameters. Section 4 shows the SCVs' water mass properties, origin, generation mechanism and volume transports. At last, Section 5 gives the summary and discussions.

2. Data and Methods

2.1. Moored data

We use five moorings from a mooring array (denoted by NS1–NS5) west of Luzon Strait to investigate SCVs (Figure 2). These five moorings were deployed

between June 2014 and June 2018 to study multiscale dynamic processes in the NESCS and associated water exchange with the NWP (Sun et al., 2020, 2022), and they are an important part of SCS mooring array system (Zhang et al., 2013). The moorings are located along 119.9 °E between latitude 19.45° to 21.96 °N with a mean spacing of ~76 km. To measure the velocity and T/S profiles continuously in nearly the full water column, each mooring is typically equipped with one upward- and one or two downward-looking 75 kHz ADCPs, several recording current meters with CTDs below, and temperature chains (composed of dozens of temperature loggers and several CTDs). Given that SCVs primarily occur in the upper 500 m, only moored data above 500 m are used here (Zhang et al., 2022). All of these instruments had a time sampling interval of 3 min. The vertical sampling interval of the ADCPs was 16 m, and the vertical resolutions of temperature chains was generally 10 or 20 m and 50 m above and below ~450 m, respectively. Most moorings and their instruments functioned well except for several occasional issues, including a malfunction of the uppermost ADCP of NS2 in the first year and a loss of the temperature chain of NS4 in the third year. As to more detailed information about these moorings, see Tables S1–S4 in the supporting material and Sun et al. (2020, 2022).

Data processing is similar to that of previous mooring-based researches (Sun et al., 2020, 2022). At first, the original velocity and temperature measurements with a temporal resolution of 3 min were averaged on an hourly basis. Then, the hourly data were linearly vertically interpolated onto a uniform grid with 5 m intervals. After that, all the moored time series were lowpass filtered (a fourth-order Butterworth filter)

with a cut-off period of 2.5 days so that tidal and near-inertial signals were effectively removed. Finally, these sub-inertial data were further daily averaged.

In the upper 500 m, there are 3–4 CTDs mounted on the temperature chain of each mooring, so the vertical resolution of salinity measurement is much coarser than the temperature. For the SCVs' water mass analysis, the CTDs-derived T/S data were processed using a different procedure, rather than the above method of the relatively sufficient temperature data. The NESCS has energetic tidal currents (especially internal tides), so that the mooring instruments typically swing and thus one or two T/S profiles per day within specific depth ranges can be obtained from each CTD. Under the assumption that T-S properties do not change within one day, we then obtained daily T/S profiles at the potential density coordinate by interpolating the original T/S data from all the CTDs at each mooring onto isopycnals from 22.0 to $27.0\sigma_0$ at an interval of $0.02\sigma_0$ (Sun et al., 2022). It should be noted that the temperature and salinity used in the following are all referred as potential temperature and practical salinity, respectively.

2.2. Other data

We also employ concurrent 1/4° daily gridded altimeter data including sea surface height (SSH) and surface absolute geostrophic velocity to help study the generation and migration processes of SCVs (http://marine.copernicus.eu/). For the NESCS, previous studies have demonstrated that the altimeter data can well capture the Kuroshio intrusion (Nan et al., 2011; Sun et al., 2020; Zhang et al., 2017). In order to calculate the volume transport through Luzon Strait, the HYCOM reanalysis data is

also used here (http://www.hycom.org/dataserver/glb-analysis). The 1/12° daily HYCOM reanalysis data contains 33 levels vertically from surface to 5500 m, 14 of which are in the upper 500 m with a resolution of 10–100 m. In addition, the 1/4° monthly and annual climatology of T/S data from the World Ocean Atlas 2018 (WOA18; Locarnini et al., 2019; Zweng et al., 2019) are analyzed in this study to compare water mass properties of SCVs with those of Kuroshio water and NESCS water and thus trace the origins of SCVs (https://www.nodc.noaa.gov/OC5/woa18/).

2.3. SCVs identification criteria

Here, we introduce the criteria to help identify SCVs in the upper 500 m from the moored data. First, the stratification or vertical temperature gradient should be enhanced for cyclones and decreased for anticyclones in the subsurface ocean. The enhanced (decreased) stratification corresponds to convex (concave) lens-shaped thermal structures, which can be directly identified from depth-time distributions of temperature. Second, vertical vortex core, defined as the location where the maximum swirl velocity occurs vertically, should be beneath the main thermocline where the maximum stratification occurs.

Third, SCVs should have a significant isopycnic salinity anomaly (S_a) relative to the local water mass. For each specific SCV, its T/S profile is obtained by averaging the T/S profiles on the isopycnals during the period when it went across the mooring. The T/S profiles of the local water mass are calculated using the WOA18 monthly climatology at mooring site. Here, the $|S_a|$ at the SCV's core should be greater than 0.03 psu, and the vertical thickness of $|S_a| > 0.02$ psu should be larger than 100 m. The

194 criteria adopted here are similar to those of Zhu et al. (2021) which investigated SCVs
195 using moorings in the Kuroshio Extension region. In the following analysis, we
196 primarily focus on the 34 SCVs that simultaneously satisfy the above three criteria
197 unless otherwise specified.

198 **2.4. Methods to estimate kinematic parameters of SCVs**

199 For each SCV, we assume that the swirl (azimuthal) velocity V within the vortex
200 maximum velocity circle obeys the theoretical distribution of a Rankine vortex (i.e.,
201 $v(r) = V_0 \frac{r}{R}$ for $r \le R$), and the migration speed U_m and direction α are constant
202 when a SCV passes a certain mooring (i.e., its center moves straightly over the short
203 term). The SCV-induced velocity anomalies u' and v' (i.e., zonal and meridional
204 components) are derived through removing background current velocity defined as
205 the time average within 5 days before and after the observed SCV. Its maximum
206 absolute velocity anomaly is taken as the maximum swirl velocity V_0,

207 $$V_0 = \left(\sqrt{u'^2 + v'^2}\right)_{\max} \quad (1)$$

208 and R is defined as the radius where the maximum velocity occurs. The background
209 current velocity and direction are approximately used to describe the migration speed
210 U_m and direction angle α (in relation to the due east direction corresponding to α
211 = 0°) of SCV (Dewar and Meng, 1995; McWilliams, 1985). According to the Rankine
212 vortex model, the nearest distance d from mooring to SCV's center is associated with
213 the minimum swirl velocity, i.e., $d = \frac{V_{\min}}{V_0} R$. Thus, the radius of SCV can be
214 calculated based on the daily swirl velocity (Δt =1 day) through

$$R = \frac{U_m \Delta t V_0}{\sqrt{V^2 - V_{\min}^2}} \quad (2)$$

Then, the theoretical value of the Rankine vortex-derived azimuthal velocity can be further deduced using

$$V = \frac{V_0 \sqrt{(U_m \Delta t)^2 + d^2}}{R} \quad (3)$$

The core depth of SCV is defined as the depth that the maximum of V_0 occurs, and the vertical length scale H_e of the SCV is defined as the depth range where the maximum of V_0 is e-folded. More details of the methods can be found in Zhang et al. (2022).

2.5. Methods to estimate Rossby and Burger numbers of SCVs

After obtaining the above-mentioned kinematic parameters of SCVs, we can further estimate the Rossby number (*Ro*) of the SCVs using

$$Ro = \frac{2V_0}{fR} \quad (4)$$

where V_0 and R are the maximum swirl velocity and radius of SCVs, respectively, and f is the local Coriolis parameter (e.g., Bosse et al., 2015). In addition, we can also estimate the Burger number (*Bu*) using

$$Bu = \frac{N^2 H_e^2}{f^2 R^2} \quad (5)$$

where H_e is the vertical length scale of SCVs (see the method in Section 2.4) and N is the average buoyancy frequency within the SCVs (e.g., Dewar and Meng, 1995; Zhang et al., 2022).

3. Kinematic Characteristics

3.1. Two cases of SCVs

Based on the methods in Section 2, we have identified a total of 34 SCVs including 25 anticyclonic SCVs and 9 cyclonic SCVs from the moored data between June 2014 and June 2018. The occurrence time and depth range of these SCVs are shown schematically in Figure 3. In order to describe the characteristics of SCVs more clearly, we first illustrate a respective example of anticyclonic and cyclonic SCVs in Figure 4 and Figure 5. These two SCVs were captured by moorings NS4 and NS2, respectively. The anticyclone (cyclone) is named A7 (C9) for short because it is the 7th (9th) anticyclonic (cyclonic) SCV captured by the moorings in chronological order. This naming method is also applied to all of the other SCVs.

It shows that A7 and C9 have convex and concave lens-shaped structures in the depth-time plots of temperature, respectively. Corresponding to their lens-shaped structures, both A7 and C9 have subsurface-intensified velocity anomalies. For the anticyclone A7, the upper- and lower-boundary isotherms of the convex lens are 10 and 17 °C, and its stratification (denoted by vertical temperature gradient) is significantly reduced. Concerning cyclone C9, the concave lens-like structure is approximately located between 10 and 22 °C isotherms and the stratification is markedly enhanced. From the depth-time plots of velocity anomalies, we see that both u' and v' of A7 change from positive to negative when it passes through the mooring NS4 (Figures 4a and 4b), while the opposite is true when C9 passes through the mooring NS2 (Figures 5a and 5b). According to the polarities of A7 and C9, we can infer that both SCVs migrated northwestward when they were observed by the moorings. The above migration direction is consistent with the direction α of the

257 background currents (i.e., 158° for A7 and 152° for C9). This consistency can be
258 found for all of the identified SCVs which further demonstrates that migration of
259 SCVs is mainly caused by the advection of background currents (Dewar and Meng,
260 1995; McWilliams, 1985).

261 For A7 (C9), the maximum velocity anomaly V_0 reaches 0.27 m s^{-1} (0.25 m s^{-1})
262 at 260 m (235 m) beneath the main thermocline, whose depth is roughly 100 m. At the
263 core depths of A7 and C9, their observed swirl velocities are in good agreement with
264 those calculated based on the Rankine vortex model (Figures 4d and 5d),
265 demonstrating the assumption of Rankine vortex applied to our parameter estimation
266 methods. It is estimated that the radius R of A7 (C9) is 48±6 km (27±6 km), and both
267 of them are less than radius of O(100) km for typical mesoscale eddies observed in
268 the NESCS (Chen et al., 2011). The vertical length scale H_e and averaged buoyancy
269 frequency N of A7 (C9) reaches 235 m and 7.6×10^{-3} s^{-1} (275 m and 1.2×10^{-2} s^{-1}),
270 respectively. On the basis of above parameters, for A7 (C9), the Rossby number Ro is
271 estimated to be –0.22 (0.35), while the Burger number Bu is estimated to be 0.55
272 (5.16). All the above parameters of A7 and C9 are generally within the scope of
273 previous descriptions of SCVs (e.g., Li et al., 2017; McWilliams, 1985). Noted that
274 the basic characteristics of A7 and C9 described here are common to all of the other
275 identified SCVs and two other examines can be found in supplementary Figures S1
276 and S2.

277 **3.2. Vertical structure of SCVs**

278 In Figure 6a, we show vertical profiles of swirl velocity for all the 34 SCVs as a

function of relative vertical distance to the vortex core (i.e., $z' = z - z_0$, where z_0 is the depth of the vortex core). For each SCV, the profile of its maximum daily swirl velocity is analyzed here. It shows that SCVs' maximum swirl velocities are generally between 0.1–0.3 m s^{-1} and their vertical length scales are between 130–280 m. At first glance, the vertical structure of swirl velocity varies substantially for different SCVs. Under the influence of depth-dependent stratification, the swirl velocity above the core depth generally decreases more rapidly with distance than that below the core depth.

In order to investigate whether the SCVs share a uniform vertical structure in terms of swirl velocity, for each SCV, we normalize the swirl velocity profile by dividing its maximum (i.e., V_0) and project it onto the stretched coordinate $z_s = \int_0^{z'} \bar{N}(z')/f \, dz'$ according to Flierl (1987) and Z.-G. Zhang et al. (2017). Here, $\bar{N}$ is the time-mean stratification during the period of each SCV. Given that SCVs have different vertical length scales, the stretched coordinate of each SCV is further normalized by dividing the corresponding e-folding vertical scale H (i.e., $H_e/2$ in the stretched coordinate). In Figure 6b, we show all profiles of the normalized swirl velocity V_n in the normalized stretched coordinate z_n. The results clearly show that $V_n(z_s)$ of the SCVs have a uniform vertical structure that shapes like a Gaussian function. This is further verified by the very close distribution between the average profile of $V_n(z_s)$ and the Gaussian function $\exp(-z_n^2)$.

3.3. Statistical characteristics of SCVs

Latitudinal and seasonal distributions of the number of SCVs are shown in

Figures 7a and 7b, respectively. It shows that SCVs are more likely to go across the central and northern parts of the mooring section. For example, eleven SCVs are being captured at NS1 (i.e., the northernmost mooring) while the number is only one at NS5 (i.e., the southernmost mooring). In addition, both anticyclonic and cyclonic SCVs have notable seasonal variations. Specifically, the number of cyclonic SCVs is largest in autumn but smallest in winter, while for anticyclonic SCVs the minimum occurs in summer. If we consider the sum of anticyclonic and cyclonic SCVs, they have the lowest occurrence possibility in summer. As will be discussed in Section 4, the above latitudinal and seasonal variations of SCVs are closely associated with their generation and migration processes, which significantly depend on the state of background currents.

The statistical distributions of SCVs' other kinematic parameters including their core depth, vertical length scale (i.e., H_e), radius (i.e., R), maximum swirl velocity (i.e., V_0), Rossby number (i.e., Ro), and Burger number (i.e., Bu) are shown in Figures 8a–8f, respectively. The detailed information of each SCV including its location, observation data, and different parameters of anticyclones and cyclones can be found in Tables S5 and S6, respectively. The majority of SCVs' core depths are located at 150–300 m, especially concentrated between 200–250 m. The core depths of anticyclonic SCVs are distributed over a relatively wide range than cyclonic SCVs. For the anticyclonic SCVs, ~80% of the estimated H_e and R values are between 130–280 m and 9–38 km, respectively, and their respective mean (median) values are 204±62 m and 26.4±13.9 km (220 m and 19.6 km). Concerning cyclonic SCVs, their

mean (median) values of H_e and R are estimated to be 188±53 m and 17.0±5.4 km (230 m and 16.4 km), respectively. These estimations suggest that in general the anticyclones are larger than cyclones; both anticyclones and cyclones are much smaller than the first baroclinic Rossby deformation radius and typical mesoscale eddies in the NESCS (Chelton et al., 1998; Chen et al., 2011; Zhang et al., 2016).

The maximum swirl velocities (i.e., V_0) of ~80% anticyclonic and all cyclonic SCVs are distributed between 0.1–0.3 m s^{-1} (Figure 8d). The mean and median value of V_0 for anticyclones (cyclones) are 0.19±0.07 and 0.18 m s^{-1} (0.19±0.07 and 0.16 m s^{-1}), respectively. The statistical results also reveal that cyclones have larger *Ro* and *Bu* than anticyclones. Specifically, all the *Ro* (*Bu*) values for cyclones exceed 0.25 (1.8), while the percentage is only 60% for anticyclones. The mean (median) *Ro* values for cyclones and anticyclones are 0.45±0.18 and –0.39±0.27 (0.42 and –0.28), respectively. With respect to the mean (median) *Bu* values, they are 4.25±2.12 and 3.62±3.31 (4.21 and 2.21) for cyclones and anticyclones, respectively. The finite to order one *Ro* and *Bu* of SCVs further demonstrate that they are indeed classified as submesoscale processes in dynamics.

Based on the kinematic parameters of SCVs, we further estimate the water volume trapped in the SCVs with the assumption that a SCV can trap the whole water mass within its vortex core (i.e., maximum velocity radius within its vertical length scale) during the migration. Given that the SCV's vertical structure exhibits a Gaussian function distribution, the volume of SCV can be obtained by:

$$Vol = \pi R^2 \int_{-H_e/2}^{H_e/2} \exp\left[-\frac{2z^2}{\left(H_e/2\right)^2} \right] dz = \left(\frac{\pi}{2} \right)^{\frac{3}{2}} H_e R^2 erf\left(\sqrt{2}\right) \approx 1.96 H_e R^2 \qquad (6)$$

where *erf* is the error function. The results show that the water volumes trapped by anticyclones (Vol_{AE}) and cyclones (Vol_{CE}) are on average $3.4\pm3.3\times10^{11}$ m^3 and $1.3\pm1.1\times10^{11}$ m^3, respectively. The above estimations are overall in order of magnitude agreement with those of Meddies (Bashmachnikov et al., 2015) and Kiddies (Li et al., 2017). Note that the Vol_{AE} is 180% larger than the Vol_{CE}, which is due to the much larger radii of anticyclones than cyclones.

4. Water Mass Transports by SCVs

4.1. Water mass properties of SCVs

Because SCVs can conserve the original water properties over a long transport distance, properties of the water mass trapped in SCVs are theoretically different from the surrounding water if they originated from nonlocal regions. To help investigate the origins of SCVs and then quantify their water mass transport, we first characterize their T-S properties here. According to Zhang et al. (2022), the SCVs observed by the moorings can be generated both in the NESCS and in the Luzon Strait. Therefore, we compare the T-S diagrams of SCVs with those of the NESCS water, the Kuroshio water, and the local water at the mooring sites. Here, T-S diagrams of SCVs are obtained from mooring CTDs derived T/S profiles within the SCVs (Zhang et al., 2022); Based on WOA18 monthly climatology, T-S diagram of Kuroshio (NESCS) is computed within the eastern (western) red squares of Figure 2, while that of local waters is computed at mooring sites.

As shown in Figure 9, the Kuroshio water is much saltier and warmer than the

NESCS water in the upper layer above ~350 m. For the Kuroshio water, its maximum salinity reaches 34.85, while it is only 34.65 for the NESCS water. Because the moorings are just west of Luzon Strait, the local water's T-S properties are between Kuroshio and NESCS waters. Through comparisons of T-S diagrams, we find that the identified 34 SCVs can be divided into two major categories according to their T-S properties (Figure 9). One category is that T-S properties of SCVs are closer to Kuroshio water and warmer and saltier than local water. The other category is the opposite, i.e., the T-S properties of SCVs are closer to NESCS water and lower and fresher than local water. For all of the 34 SCVs, 84% of the anticyclones (i.e., 21/25) and 100% of the cyclones (i.e., 9/9) trap water mass close to the Kuroshio water. This result suggests that 88% (i.e., 30/34) of these SCVs trap Kuroshio water and their generations must be closely associated with the Kuroshio. Given that only the SCVs trapping Kuroshio water can contribute to NESCS-NWP subsurface water mass transports, we will primarily focus on this major category of SCVs (i.e., the first category) in the following analysis.

4.2. Origin and generation of SCVs

After SCVs are generated, they migrate under the advection of background currents with their water properties being to a large degree conserved (McWilliams, 1985). Based on this truth, we can roughly infer the origin of each SCV by tracing the salinity within its core along isopycnal surface by combing the WOA18 monthly climatology (e.g., Zhang et al., 2015). Similar to the anticyclonic SCV reported in Zhang et al. (2022), the results of water mass tracing reveal that the origins of 30

SCVs trapping Kuroshio water (i.e., the first category) are most likely to locate in the southern Luzon Strait. In order to verify this point, we further examine the spatial distributions of altimeter-derived SSH and surface geostrophic currents during the periods when and before each specific SCV was observed by the mooring. We find that for all of the 30 SCVs, the Kuroshio evidently intruded into the NESCS when and (up to one month) before the SCVs were observed, in the form of either a leaking path or looping path (Figure 10 and Figures S3–S6). The Kuroshio went through southern Luzon Strait (specifically, Babuyan Islands) and its main axis or branch directly extended to the mooring that captured a SCV. This is in great contrast to the leaping path of Kuroshio, during which period no SCVs were observed (Figures 10g–10i). The patterns of Kuroshio intrusion further demonstrate that these SCVs trapping Kuroshio water are generated near the Babuyan Islands (recall Figure 2).

The above SCVs' T-S characteristics and generation sites are very similar to the anticyclonic SCV reported by Zhang et al. (2022). Therefore, we think these SCVs are also generated through interactions between Kuroshio and the complex topography of the Babuyan Islands. This generation mechanism (i.e., current-topography interaction) which feeds SCVs through horizontal shear instability of background currents (vorticity generated by frictional effects) is actually believed as one of the major generation mechanisms in the ocean (e.g., D'Asaro, 1988; Gula et al., 2019; Molemaker et al., 2015; Srinivasan et al., 2019). Different from the observation of Zhang et al. (2022), however, we propose that both anticyclones and cyclones are able to be formed during the interaction between Kuroshio and Babuyan Islands. In the

Kuroshio flowing direction, anticyclones (cyclones) are generated on the left (right) side of the island, which produces anticyclonic (cyclonic) shear due to topographic frictions (Figure 11b). In such generation process, the anticyclones southwest of the island (i.e., left side) are more likely to migrate into the NESCS by the intruding Kuroshio while the cyclones on the opposite side tend to be advected into NWP by the northward flowing branch of the Kuroshio. This partly explains why there are more anticyclones than cyclones being captured by the moorings. In addition, the smaller scale of cyclones than anticyclones means that they are more difficult to be captured by moorings, which provides another potential explanation for the polarity skewness observed here (Zhang et al., 2022). Given that this category of SCVs commonly occurs in the wake of islands in the Luzon Strait, we propose to name them Luzon Strait island wake eddies, i.e., Liddies for short.

4.3. Volume transports by SCVs

Given that the space between two neighbor moorings (i.e., the mean distance of 76 km) is larger than the radius of the SCVs, in addition to the identified 30 Liddies that transport Kuroshio water into the NESCS, there should be some similar SCVs (i.e., some additional Liddies) that had been missed by the moorings. In order to estimate the real westward volume transport caused by Liddies, we further estimate the total number of Liddies that go across the mooring section. The kinematic parameters of SCVs (Tables S5 and S6; Figure S7) reveal that all values of d/R are less than 1/2 (the maximum ratio is 0.43; here, d is the nearest distance between the mooring and the center of a SCV). According to this fact, we further assume that our

criteria in Section 2.3 can only identify the SCVs with $d/R \le 1/2$. Based on this assumption, we can then estimate the total number of Liddies passing through the mooring array from the perspective of probability and geometric relationship (see Figure A1) using Equations 7 and 8,

$$N_{AE} = \sum_{i=1}^{6} N_{AE}^{i} = \sum_{i=1}^{6} r\cos\beta / \bar{R}_{AE}^{i} \cdot n_{AE}^{i} \quad (7)$$

$$N_{CE} = \sum_{i=1}^{6} N_{CE}^{i} = \sum_{i=1}^{6} r\cos\beta / \bar{R}_{CE}^{i} \cdot n_{CE}^{i} \quad (8)$$

Here, r=76 km is mean spacing of two neighboring moorings, β=35° is mean migration angle of the identified Liddies relative to the westward direction (Figure A1), $\bar{R}_{AE}^{i}$ ($\bar{R}_{CE}^{i}$) is the mean radius of the identified anticyclonic (cyclonic) Liddies in a certain radius range between 0 and 60 km with an interval of 10 km (e.g., i=1 and i=6 mean the ranges of 0–10 km and 50–60 km, respectively), and n_{AE}^{i} (n_{CE}^{i}) is the number of the identified anticyclonic (cyclonic) Liddies within that radius range. So, $r\cos\beta$=62.4 km is defined as "effective distance" of two neighboring moorings perpendicular to mean migration direction of Liddies (Figure A1). Taking the above parameters into Equations 7 and 8, we finally conclude that there is a total of 59 anticyclonic and 35 cyclonic Liddies that had migrated across the mooring section during the ~4 years observation period.

Based on the total number of Liddies mentioned above, we further estimate the equivalent annual-mean westward volume transport caused by Liddies using

$$Transport = \left(\overline{Vol_{AE}} \cdot N_{AE} + \overline{Vol_{CE}} \cdot N_{CE}\right) / \Delta t \quad (9)$$

where $\overline{Vol_{AE}}$ ($\overline{Vol_{CE}}$) is the volume of anticyclonic (cyclonic) SCVs and Δt =4

453 years is the entire observation duration. So, the total volume transport by the Liddies
454 is estimated to be 0.20 Sv (1 Sv equals 10^6 m^3 s^{-1}). Based on the concurrent 1/12°
455 HYCOM reanalysis data, mean volume transport across the Luzon Strait (i.e., the
456 120.8°E section between Luzon and Taiwan Islands) between 100–400 m, i.e., the
457 layer of SCVs, is estimated to be 3.31 Sv. This result means that the Liddies-induced
458 westward volume transport accounts for 6.0% of the Luzon Strait transport in the
459 subsurface layer between 100–400 m, which suggests that Liddies play a
460 nonnegligible role in the NESCS-NWP subsurface water transports.

461 **5. Summary and Discussions**

462 Using concurrent velocity, temperature, and salinity observations from five
463 moorings between June 2014 and June 2018, we have identified 34 SCVs including
464 25 anticyclones and 9 cyclones west of Luzon Strait in the NESCS. The core depths
465 of SCVs' are generally located at between 150–300 m depths and they tend to more
466 frequently occur in the central and northern part of the mooring section west of Luzon
467 Strait. Seasonally, the SCVs have the lowest occurrence frequency in summer than
468 other seasons. For anticyclonic (cyclonic) SCVs, their mean radius, maximum swirl
469 velocity, vertical length scale, Rossby number, and Burger number are calculated to
470 be 26.4±13.9 km (17.0±5.4 km), 0.19±0.07 m s^{-1} (0.19±0.07 m s^{-1}), 204±62 m
471 (188±53 m), –0.39±0.27 (0.45±0.18), and 3.62±3.31 (4.25±2.12), respectively. The
472 smaller scale compared with the first baroclinic Rossby deformation radius and the
473 Rossby and Burger numbers from finite to order one demonstrate that the SCVs
474 observed here are in the category of submesoscale processes in dynamics. In addition,

we find that the swirl velocities of SCVs conform to the Gaussian function in the vertical direction in stretching coordinates (i.e., removing the influence of stratification).

Water mass analysis suggests that 30 SCVs trap water mass close to Kuroshio water and only 4 anticyclonic SCVs trap the NESCS water. Through the combination of water mass tracing on isopycnal surface and distributions of background circulations, we demonstrate the SCVs trapping Kuroshio water are generated in the wakes of Babuyan Islands (within southern Luzon Strait) and their generation mechanism is Kuroshio-islands interactions as proposed by Zhang et al. (2022). Given the common origin and generation mechanism of this kind of SCVs, we term them as the Luzon Strait island wake eddies, Liddies for short. From the perspective of probability and geometry when SCVs migrate across the mooring section, we estimate that during the 4-year observation period, there are another 64 Liddies that should have entered the NESCS but have been missed by the moorings and identification criteria. If all of these Liddies are considered, they can result in an equivalent annual-mean volume transport of 0.20 Sv westward into the NESCS, which accounts for 6.0% of the Luzon Strait transport in the subsurface layer between 100–400 m.

Given the considerable westward volume transports by Liddies, their generations and migrations provide a novel route for the Pacific water to enter the NESCS. Because the Kuroshio water and thus the tracers trapped in the SCVs are more conserved than those associated with the Kuroshio intrusion itself, the Liddies may play a unique and potentially important role in modulating the biogeochemical

processes in the NESCS, which should be taken into account in future studies. In addition to the Liddies reported here, given the strong circulation and mesoscale eddies and complex topography in the SCS, SCVs generated through current-topography interaction should commonly exist in the SCS, which needs to be confirmed using more high-resolution targeted observations. Finally, generations of SCVs through Kuroshio-islands interactions provide an efficient route of direct energy cascade for the Kuroshio. Note that similar SCVs' generation processes have also been observed in other western boundary currents (Gula et al., 2019; Lazaneo et al., 2022). Given this, SCVs may play an important role in the dissipation of western boundary currents, which need to be evaluated in the future.

Acknowledgement

This study is jointly supported by the National Natural Science Foundation of China (42222601, 92258301, 42076004) and the 2022 Research Program of Sanya Yazhou Bay Science and Technology City (SKJC-2022-01-001). Z. Zhang is also supported by the "Taishan" Talents program (tsqn202103032) and Shandong Provincial Natural Science Foundation (ZR2023JQ013).

Data Availability Statement

The moored data analyzed in this study can be obtained online at https://doi.org/10.7910/DVN/4YCNW3. The gridded altimeter data, HYCOM reanalysis data, and monthly and annual WOA18 climatology can be downloaded from http://marine.copernicus.eu/, http://www.hycom.org/dataserver/glb-analysis, and https://www.nodc.noaa.gov/OC5/woa18/, respectively.

Appendix A: The geometric relationship for the estimation of the total number of Liddies passing through the mooring array.

In the following, we use a schematic diagram to display the geometric relationship for the estimation of the total number of Liddies passing through the mooring array. Without loss of generality, we choose two neighboring moorings along the mooring section (119.9 °E) to demonstrate the geometric relationship between their spacing (*r*, i.e., ~76 km) and the radius (*R*) of a SCV. The SCV's radius, migration direction, and effective distance ($r\cos\beta$) used in Section 4.3 are also shown in Figure A1. It's important to note that we assume that the morrings only capture the SCVs with $d/R \le 1/2$.

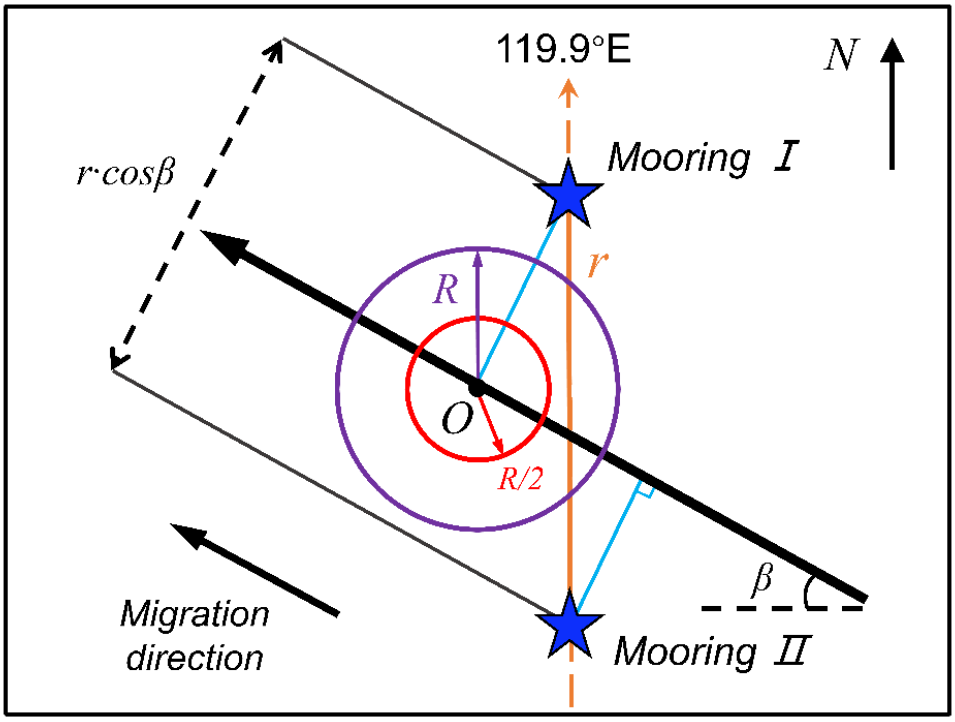

Figure A1. Schematic diagram of a SCV entering the NESCS through the mooring gap. Here, blue stars denote the moorings, r represents spacing of two neighboring moorings, β indicates migration angle of SCV, R is SCV's radius, and $1/2R$ is the critical value when the SCV can be identified by our criteria in Section 2.3. The north direction is marked in the upper right corner.

References

Adams, K. A., Hosegood, P., Taylor, J. R., Sallée, J.-B., Bachman, S., Torres, R., & Stamper, M. (2017). Frontal circulation and submesoscale variability during the formation of a Southern Ocean mesoscale eddy. *Journal of Physical Oceanography*, *47*(7), 1737–1753. https://doi.org/10.1175/JPO-D-16-0266.1

Bashmachnikov, I., Neves, F., Calheiros, T., & Carton, X. (2015). Properties and pathways of Mediterranean water eddies in the Atlantic. *Progress in Oceanography*, *137*, 149–172. https://doi.org/10.1016/j.pocean.2015.06.001

Bosse, A., Testor, P., Mortier, L., Prieur, L., Taillandier, V., d'Ortenzio, F., & Coppola, L. (2015). Spreading of Levantine intermediate waters by submesoscale coherent vortices in the northwestern Mediterranean Sea as observed with gliders. *Journal of Geophysical Research: Oceans*, *120*, 1599–1622. https://doi.org/10.1002/2014JC010263

Bosse, A., Testor, P., Mayot, N., Prieur, L., D'Ortenzio, F., Mortier, L., & Raimbault, P. (2017). A submesoscale coherent vortex in the Ligurian Sea: From dynamical barriers to biological implications. *Journal of Geophysical Research: Oceans*, *122*, 6196–6217. https://doi.org/10.1002/2016JC012634

Bower, A. S., Armi, L., & Ambar, I. (1997). Lagrangian observations of Meddy formation during a Mediterranean Undercurrent seeding experiment, *Journal of Physical Oceanography*, *27*(12), 2545–2575. https://doi.org/10.1175/1520-0485(1997)027<2545:LOOMFD>2.0.CO;2

Bower, A. S., Hendry, R. M., Amrhein, D. E., & Lilly, J. M. (2013). Direct observations of formation and propagation of subpolar eddies into the subtropical North Atlantic. *Deep Sea Research Part II: Topical Studies in Oceanography*, *85*, 15–41. https://doi.org/10.1016/j.dsr2.2012.07.029

Cao, H., Jing, Z., Fox-Kemper, B., Yan, T., & Qi, Y. (2019). Scale transition from geostrophic motions to internal waves in the northern South China Sea. *Journal of Geophysical Research: Oceans*, *124*, 9364–9383. https://doi.org/10.1029/2019JC015575

Chelton, D. B., Deszoeke, R. A., Schlax, M. G., El Naggar, K., & Siwertz, N. (1998). Geographical variability of the first baroclinic Rossby radius of deformation. *Journal of Physical Oceanography*, *28*(3), 433–460.

https://doi.org/10.1175/1520-0485(1998)028<0433:GVOTFB>2.0.CO;2

Chen, G., Hou, Y., & Chu, X. (2011). Mesoscale eddies in the South China Sea: Mean properties, spatiotemporal variability, and impact on thermohaline structure. *Journal of Geophysical Research: Oceans*, *116*, C06018. https://doi.org/10.1029/2010JC006716

Collins, C. A., Margolina, T., Rago, T. A., & Ivanov, L. (2013). Looping RAFOS floats in the California current system. *Deep Sea Research Part II: Topical Studies in Oceanography*, *85*, 42–61. https://doi.org/10.1016/j.dsr2.2012.07.027

D'Asaro, E. A. (1988). Generation of submesoscale vortices: A new mechanism. *Journal of Geophysical Research: Oceans*, *93*, 6685. https://doi.org/10.1029/JC093iC06p06685

Dewar, W. K., & Meng, H. (1995). The propagation of submesoscale coherent vortices. *Journal of Physical Oceanography*, *25*(8), 1745–1770. https://doi.org/10.1175/1520-0485(1995)025,1745:TPOSCV.2.0.CO;2

Dong, J., & Zhong, Y. (2018). The spatiotemporal features of submesoscale processes in the northeastern South China Sea. *Acta Oceanologica Sinica*, *37*(11), 8–18. https://doi.org/10.1007/s13131-018-1277-2

Dong, J., Fox-Kemper, B., Jing, Z., Yang, Q., Tian, J., & Dong, C. (2022). Turbulent dissipation in the surface mixed layer of an anticyclonic mesoscale eddy in the South China Sea. *Geophysical Research Letters*, *49*, e2022GL100016. https://doi.org/10.1029/2022GL100016

Frenger, I., Bianchi, D., Stührenberg, C., Oschlies, A., Dunne, J., Deutsch, C., Galbraith, E., & Schütte, F. (2018). Biogeochemical role of subsurface coherent eddies in the ocean: Tracer cannonballs, hypoxic storms, and microbial stewpots? *Global Biogeochemical Cycles*, *32*, 226–249. https://doi.org/10.1002/2017GB005743

Flierl, G. R. (1987). Isolated eddy models in geophysics. *Annual Review of Fluid Mechanics*, *19*, 493–530. https://doi.org/10.1146/annurev.fl.19.010187.002425

Garfield, N., Collins, C. A., Paquette, R. G., & Carter, E. (1999). Lagrangian exploration of the California undercurrent, 1992–95. *Journal of Physical Oceanography*, *29*(4), 560–583. https://doi.org/10.1175/1520-0485(1999)029<0560:LEOTCU>2.0.CO;2

Gula, J., Blacic, T. M., & Todd, R. E. (2019). Submesoscale coherent vortices in the Gulf Stream. *Geophysical Research Letters*, *46*, 2704–2714. https://doi.org/10.1029/2019GL081919

Gula, J., Taylor, J., Shcherbina, A., & Mahadevan, A. (2021). Submesoscale processes and mixing.

In *Ocean Mixing* (pp. 181–214). https://doi.org/10.1016/B978-0-12-821512-8.00015-3

Lazaneo, C. Z., Calil, P. H. R., Tandon, A., & da Silveira, I. C. A. (2022). Submesoscale coherent vortices in the South Atlantic Ocean: A pathway for energy dissipation. *Journal of Geophysical Research: Oceans*, *127*, e2020JC017099. https://doi.org/10.1029/2020JC017099

Li, C., Zhang, Z., Zhao, W., & Tian, J. (2017). A statistical study on the subthermocline submesoscale eddies in the northwestern Pacific Ocean based on Argo data. *Journal of Geophysical Research: Oceans*, *122*, 3586–3598. https://doi.org/10.1002/2016JC012561

Lin, H., Liu, Z., Hu, J., Menemenlis, D., & Huang, Y. (2020). Characterizing meso- to submesoscale features in the South China Sea. *Progress in Oceanography*, *188*, 102420. https://doi.org/10.1016/j.pocean.2020.102420

Locarnini, R. A., Mishonov, A., Baranova, O., Boyer, T., Zweng, M., Garcia, H., et al. (2019). World Ocean Atlas 2018, volume 1: Temperature. In A. Mishonov (Ed.), *NOAA Atlas NESDIS 81* (Vol 1, pp. 52). Silver Spring, MD: NOAA.

McCoy, D., Bianchi, D., & Stewart, A. L. (2020). Global observations of submesoscale coherent vortices in the ocean, *Progress in Oceanography*, *189*, 102452. https://doi.org/10.1016/j.pocean.2020.102452

McDowell, S. E., & Rossby, H. T. (1978). Mediterranean water: An intense mesoscale eddy off the Bahamas, *Science*, *202*(4372), 1085–1087. https://doi.org/10.1126/science.202.4372.1085

McWilliams, J. C. (1985). Submesoscale, coherent vortices in the ocean. *Reviews of Geophysics*, *23*(2), 165–182. https://doi.org/10.1029/RG023i002p00165

McWilliams, J. C. (2016). Submesoscale currents in the ocean. *Proceedings of the Royal Society A*, *472*(2189), 20160117. https://doi.org/10.1098/rspa.2016.0117

Molemaker, M. J., McWilliams, J. C., & Dewar, W. K. (2015). Submesoscale instability and generation of mesoscale anticyclones near a separation of the California Undercurrent. *Journal of Physical Oceanography*, *45*(3), 613–629. https://doi.org/10.1175/JPO-D-13-0225.1

Nan, F., Xue, H., Chai, F., Shi, L., Shi, M., & Guo, P. (2011). Identification of different types of Kuroshio intrusion into the South China Sea. *Ocean Dynamics*, *61*, 1291–1304. https://doi.org/10.1007/s10236-011-0426-3

Pelland, N. A., Eriksen, C. C., & Lee, C. M. (2013). Subthermocline Eddies over the Washington

626 Continental Slope as Observed by Seagliders, 2003-09. *Journal of Physical Oceanography*,
627 *43*(10), 2025–2053. https://doi.org/10.1175/JPO-D-12-086.1
628 Richardson, P. L., Price, J. F., Walsh, D., Armi, L., & Schröder, M. (1989). Tracking three meddies
629 with SOFAR floats. *Journal of Physical Oceanography*, *19*(3), 371–383.
630 https://doi.org/10.1175/1520-0485(1989)019<0371:TTMWSF>2.0.CO;2
631 Richardson, P. L., McCartney, M. S., & Malliard, C. (1991). A search for Meddies in historical
632 data. *Dynamics of Atmospheres and Oceans*, *15*(3–5), 241–265.
633 https://doi.org/10.1016/0377-0265(91)90022-8
634 Song, X., Xie, X., Qiu, B., Cao, H., Xie, S.-P., Chen, Z., & Yu, W. (2022). Air-Sea Latent Heat
635 Flux Anomalies Induced by Oceanic Submesoscale Processes: An Observational Case Study.
636 *Frontiers in Marine Science*, *9*, 850207. https://doi.org/10.3389/fmars.2022.850207
637 Srinivasan, K., McWilliams, J. C., Molemaker, M. J., & Barkan, R. (2019). Submesoscale vortical
638 wakes in the lee of topography. *Journal of Physical Oceanography*, *49*(7), 1949–1971.
639 https://doi.org/10.1175/JPO-D-18-0042.1
640 Steinberg, J. M., Pelland, N. A., & Eriksen, C. C. (2019). Observed Evolution of a California
641 Undercurrent Eddy. *Journal of Physical Oceanography*, *49*(3), 649–674.
642 https://doi.org/10.1175/JPO-D-18-0033.1
643 Sun, Z., Zhang, Z., Qiu, B., Zhang, X., Zhou, C., Huang, X., Zhao, W., & Tian, J. (2020).
644 Three-Dimensional Structure and Interannual Variability of the Kuroshio Loop Current in the
645 Northeastern South China Sea. *Journal of Physical Oceanography*, *50*(9), 2437–2455.
646 https://doi.org/10.1175/JPO-D-20-0058.1
647 Sun, Z., Zhang, Z., Qiu, B., Zhou, C., Zhao, W., & Tian, J. (2022). Subsurface mesoscale eddies
648 observed in the northeastern South China Sea: Dynamic features and water mass transport.
649 *Journal of Physical Oceanography*, *52*(5), 841–855.
650 https://doi.org/10.1175/JPO-D-21-0177.1
651 Taylor, J. R., & Thompson, A. F. (2023). Submesoscale dynamics in the upper ocean. *Annual*
652 *Review of Fluid*
653 *Mechanics*, *55*, 103– 127. https://doi.org/10.1146/annurev-fluid-031422-095147
654 Torres, H. S., & Gomez-Valdes, J. (2017), Erosion of a California Undercurrent eddy by bottom
655 topography, *Journal of Geophysical Research: Oceans*, *122*, 3715–3735.

https://doi.org/10.1002/2016JC011870

Zhang, X., Zhang, Z., McWilliams, J. C., Sun, Z., Zhao, W., & Tian, J. (2022). Submesoscale coherent vortices observed in the northeastern South China Sea. *Journal of Geophysical Research: Oceans*, *127*, e2021JC018117. https://doi.org/10.1029/2021JC018117

Zhang, Z.-G., Zhang, Y., & Wang, W. (2017). Three-compartment structure of subsurface-intensified mesoscale eddies in the ocean. *Journal of Geophysical Research: Oceans*, *122*, 1653–1664. https://doi.org/10.1002/2016JC012376

Zhang, Z.-W., Zhao, W., Tian, J., & Liang, X. (2013). A mesoscale eddy pair southwest of Taiwan and its influence on deep circulation. *Journal of Geophysical Research: Oceans*, *118*, 6479–6494. https://doi.org/10.1002/2013JC008994

Zhang, Z.-W., Li, P., Xu, L., Li, C., Zhao, W., Tian, J., & Qu, T. (2015). Subthermocline eddies observed by rapid‐sampling Argo floats in the subtropical northwestern Pacific Ocean in spring 2014. *Geophysical Research Letters*, *42*, 6438–6445. https://doi.org/10.1002/2015GL064601

Zhang, Z.-W., Tian, J., Qiu, B., Zhao, W., Chang, P., Wu, D., & Wan, X. (2016). Observed 3D structure, generation, and dissipation of oceanic mesoscale eddies in the South China Sea. *Scientific Reports*, *6*, 24349. https://doi.org/10.1038/srep24349

Zhang, Z.-W., Zhang, Y., Qiu, B., Sasaki, H., Sun, Z., Zhang, X., et al. (2020). Spatiotemporal characteristics and generation mechanisms of submesoscale currents in the northeastern South China Sea revealed by numerical simulations. *Journal of Geophysical Research: Oceans*, *125*, e2019JC015404. https://doi.org/10.1029/2019JC015404

Zhang, Z.-W., Zhang, X., Qiu, B., Zhao, W., Zhou C., Huang, X., et al. (2021). Submesoscale currents in the subtropical upper ocean observed by long-term high-resolution mooring arrays. *Journal of Physical Oceanography*, *51*(1), 187–206. https://doi.org/10.1175/JPO-D-20-0100.1

Zhang, Z.-W., Zhao, W., Qiu, B., & Tian, J. (2017). Anticyclonic eddy sheddings from Kuroshio loop and the accompanying cyclonic eddy in the northeastern South China Sea. *Journal of Physical Oceanography*, *47*(6), 1243–1259. https://doi.org/10.1175/JPO-D-16-0185.1

Zhong, Y., Bracco, A., Tian, J., Dong, J., Zhao, W., & Zhang, Z. (2017). Observed and simulated submesoscale vertical pump of an anticyclonic eddy in the South China Sea. *Scientific*

Reports, *7*, 44011. https://doi.org/10.1038/srep44011

Zhu, R., Chen, Z., Zhang, Z., Yang, H., & Wu, L. (2021). Subthermocline eddies in the Kuroshio Extension region observed by mooring arrays. *Journal of Physical Oceanography*, *51*(2), 439–455. https://doi.org/10.1175/JPO-D-20-0047.1

Zweng, M. M., Reagan, J., Seidov, D., Boyer, T., Locarnini, R., Garcia, H., et al. (2019). World Ocean Atlas 2018, volume 2: Salinity. In A. Mishonov (Ed.), *NOAA Atlas NESDIS 82* (Vol. 2, pp. 50). NOAA.

Figures

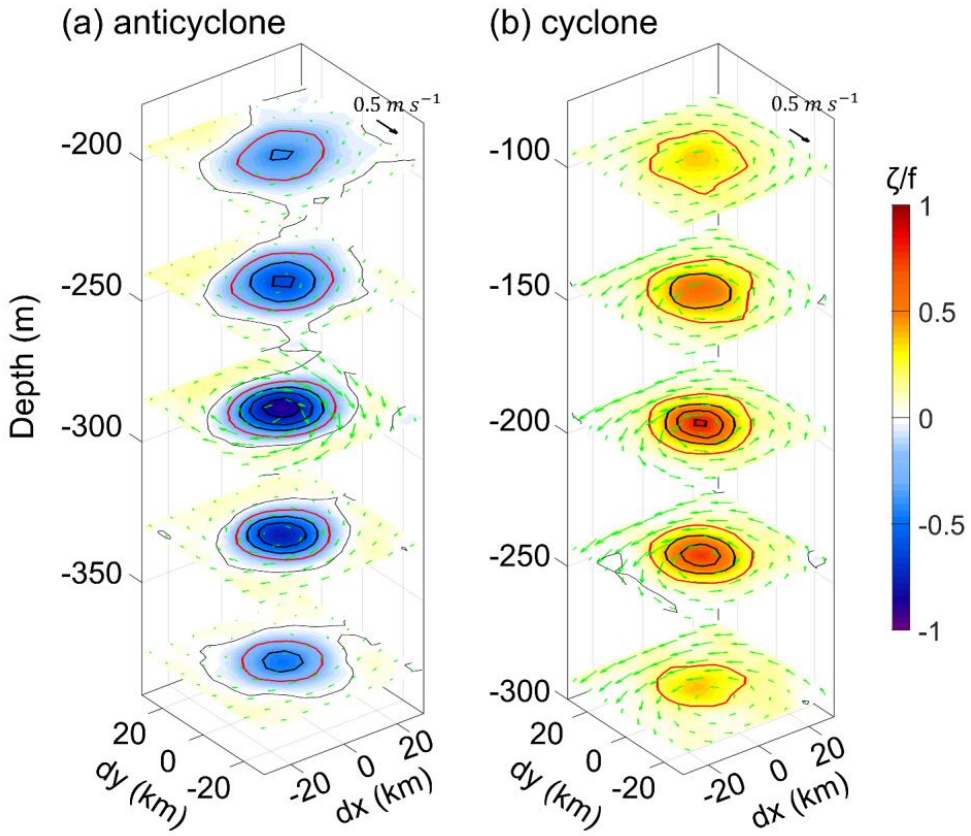

Figure 1. Three-dimensional structures of (a) anticyclonic and (b) cyclonic SCVs in the northeastern South China Sea (NESCS) reproduced using the MITgcm LLC4320 simulation. Shading and gray arrows denote the Rossby number (i.e., normalized relative vorticity or ζ/f) and velocity vectors, respectively. Black thick lines denote the contours of the Rossby number with an interval of 0.2, among which the zero and ±0.2 are indicated using thin black lines and thick red lines, respectively.

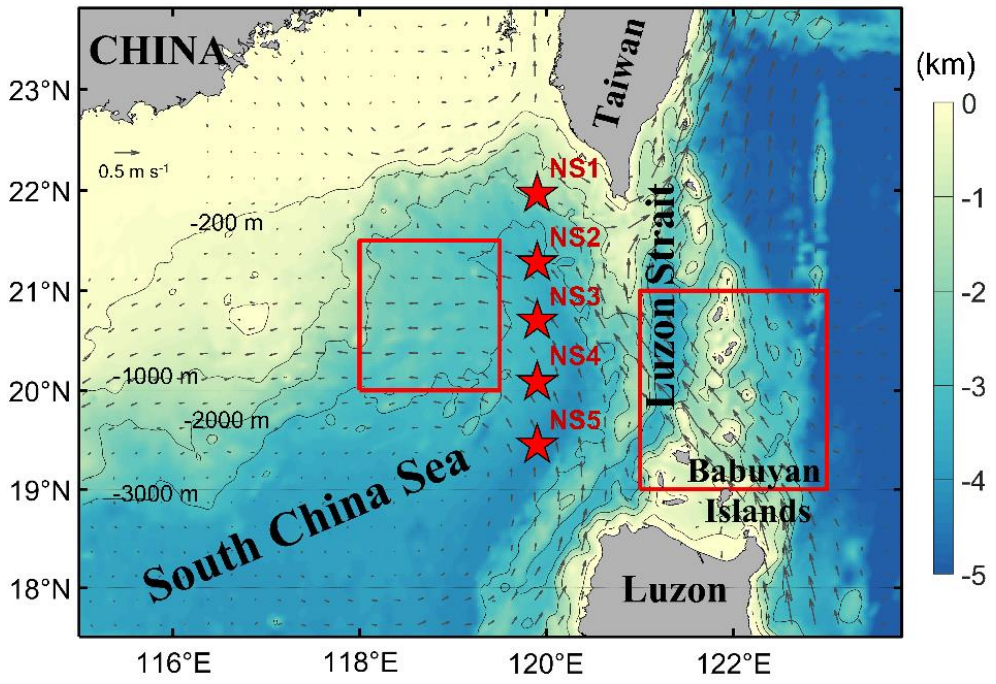

704

705 **Figure 2.** Bathymetry (color shading) and NS1–NS5 moorings location (red
706 pentagrams) in the NESCS. Gray vectors denote the mean altimeter absolute
707 geostrophic velocities from 2014 to 2018. Two red squares from west to east denote
708 the regions used for characterizing background T-S properties of NESCS water
709 (118.0°–119.5°E, 20.0°–21.5°N) and Kuroshio water (121.0°–123.0°E, 19.0°–21.0°N),
710 respectively. Black lines indicate the 200 m, 1000 m, 2000 m, and 3000 m isobaths.

711

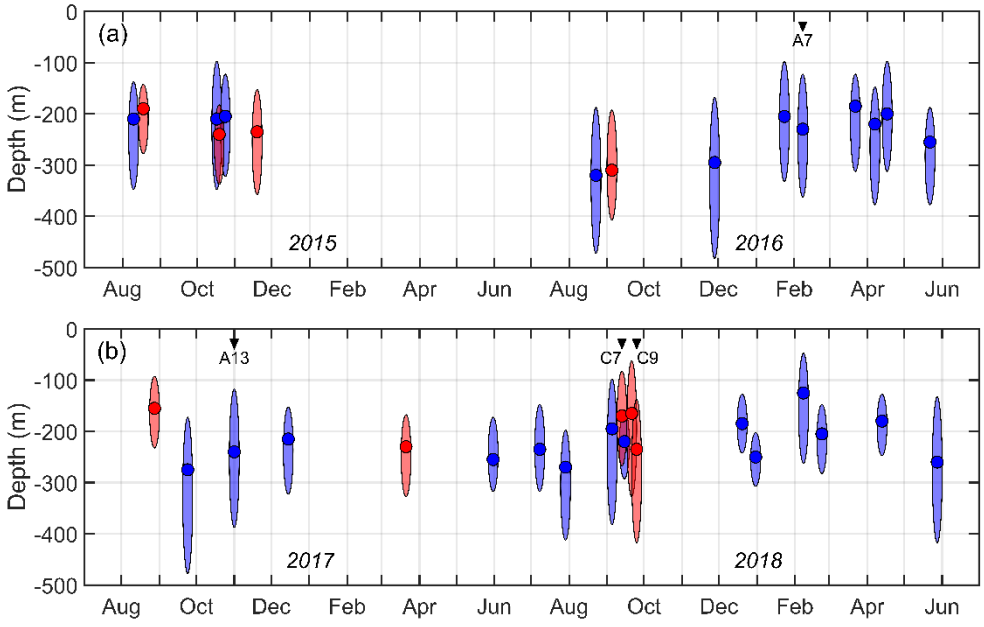

712

713 **Figure 3.** The occurrence time and depth range of SCVs observed at the moorings (a)

714 from July 2014 to June 2016 and (b) from July 2016 to June 2018. The blue (red)

715 ellipses represent the anticyclones (cyclones). Core depths of anticyclones (cyclones)

716 are indicated using blue (red) solid circles. 4 SCV cases presented in the main text and

717 online supplemental material are marked using black inverted triangles.

718

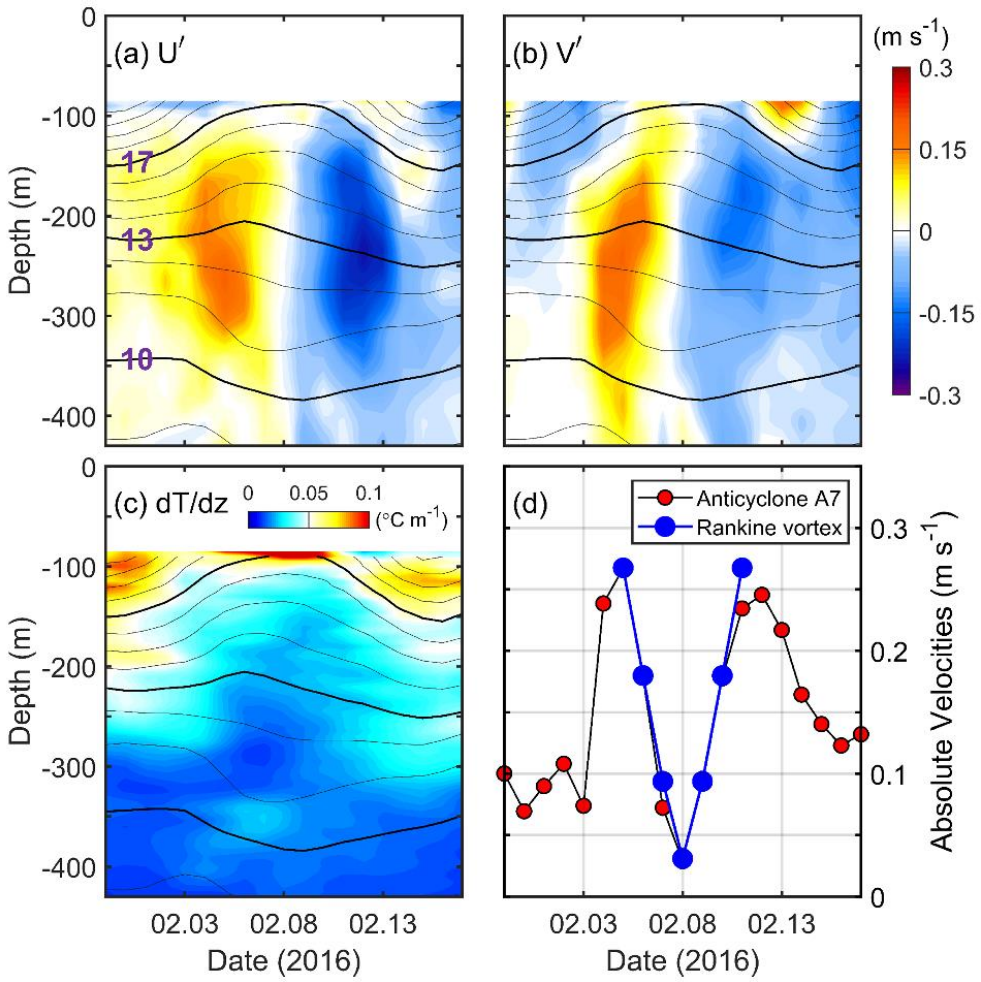

719

720 **Figure 4.** (a–c) Depth-time plots of zonal and meridional velocity anomalies and
721 vertical temperature gradient at mooring NS4 during the period of the 7th anticyclonic
722 SCV (30 January to 17 February 2016). Black thin lines indicate temperature isolines
723 with an interval of 1 °C, and three black thick lines are the 10, 13, and 17 °C
724 isotherms. (d) Comparison of the NS4-observed absolute velocity anomalies of the
725 anticyclone (red dots) and the azimuthal velocities derived from Rankine vortex (blue
726 dots; see the method in Section 2.4).

727

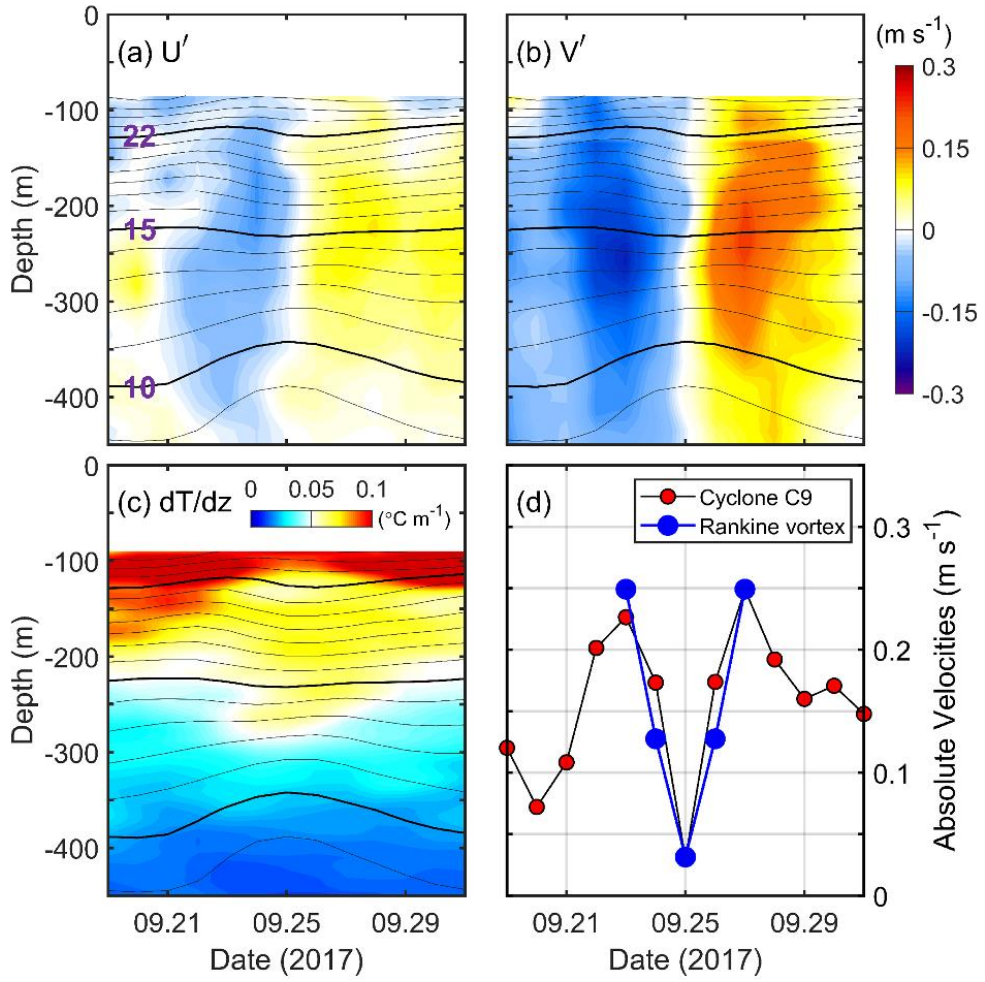

728

729 **Figure 5.** Same as Figure 4 but for the 9th cyclonic SCV (19 September to 1 October

730 2017) observed at mooring NS2. And three thick lines are the 10, 15, and 22 °C

731 isotherms.

732

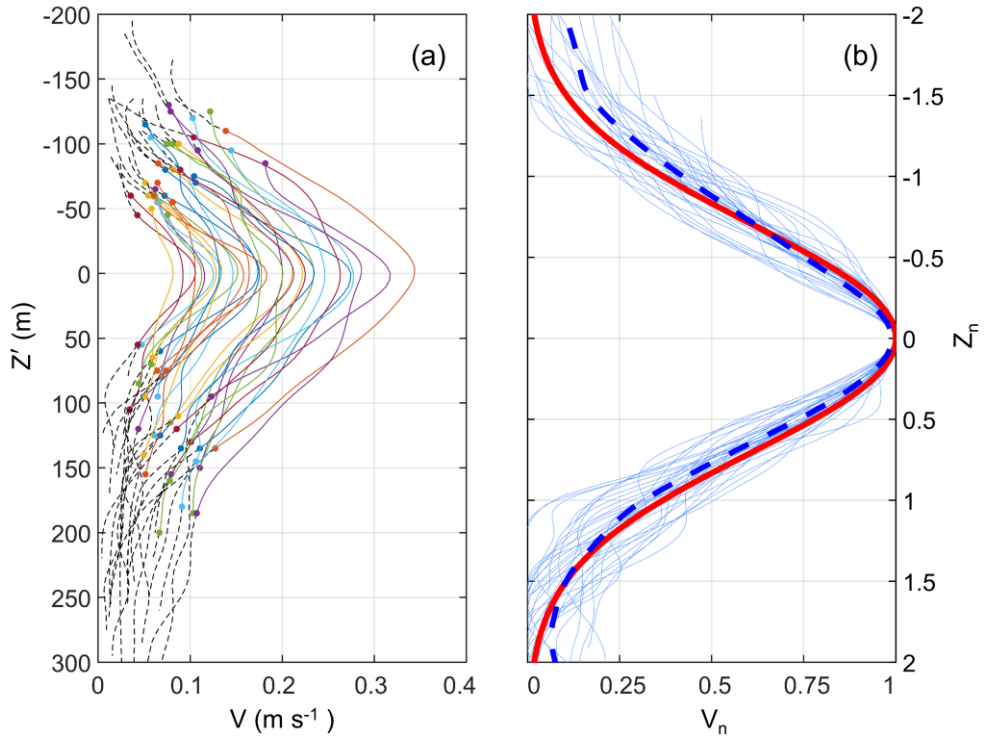

733

734 **Figure 6.** (a) Vertical profiles of swirl velocity for all SCVs as a function of relative

735 vertical distance to the vortex core depth. Different SCVs are denoted using different

736 colored lines. The two dots in each line show the e-folding vertical scale of each SCV.

737 Thin black dashed lines indicate the velocities outside the e-folding scales. (b)

738 Vertical profiles of normalized absolute velocity anomaly in normalized stretched

739 coordinates z_n (i.e., z_s/H). Blue thin solid lines denote the results of all observed

740 SCVs, while blue thick dashed line denotes mean result of them. Red thick solid line

741 denotes the fitting result of a Gaussian function (i.e., $V_n = \exp\left(-z_n^2\right)$).

742

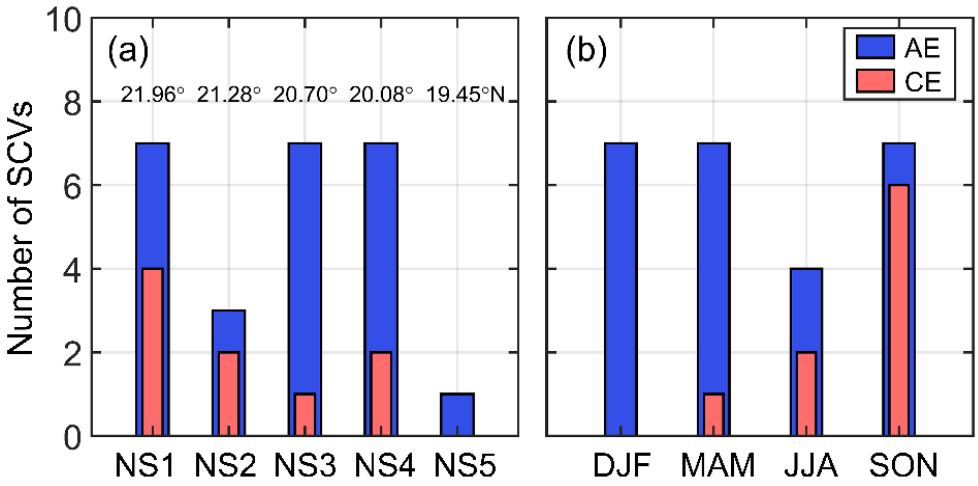

743

744 **Figure 7.** Statistical results of (a) the number of SCVs passing through different

745 moorings and (b) the number of SCVs' occurrences in different seasons. The latitudes

746 of the corresponding moorings are marked. The blue and red bars indicate

747 anticyclonic and cyclonic SCVs, respectively.

748

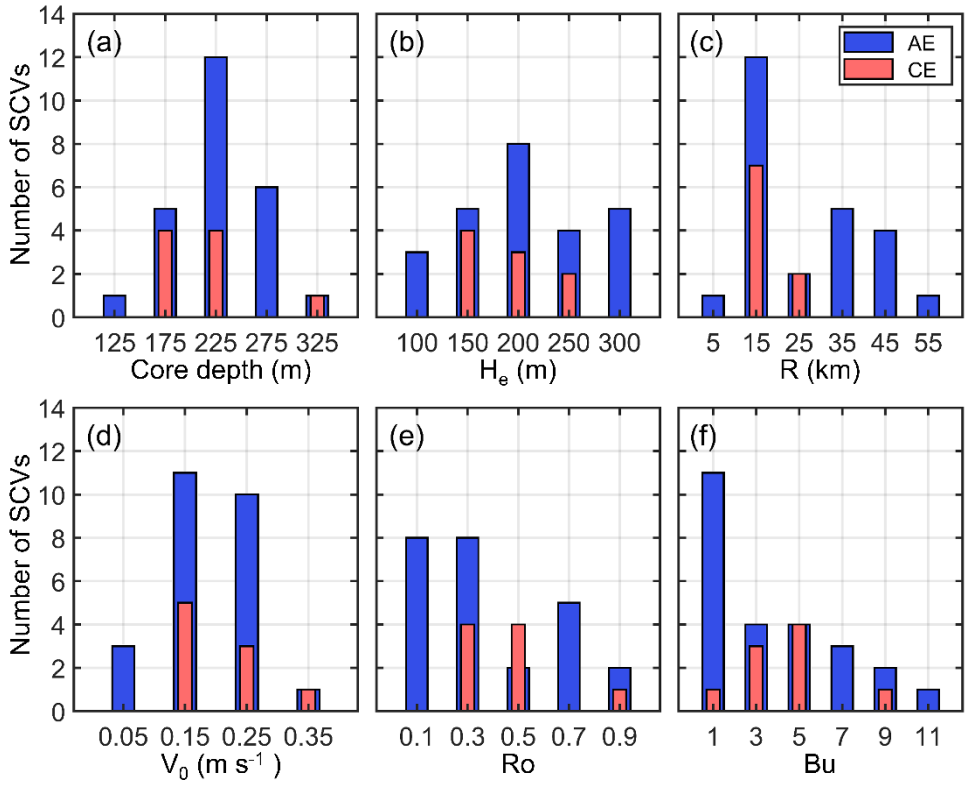

Figure 8. Same with Figure 7 but for other parameters of SCVs including (a) core depth, (b) vertical length scale H_e, (c) radius R, (d) maximum swirl velocity V_0, (e) Rossby number Ro, and (f) Burger number Bu. The x-label value represents the number of SCVs within the corresponding interval range around a center value (e.g., 225 in Figure 8a represents the number of SCVs with a core depth between 200–250 m). Blue and red bars denote anticyclonic and cyclonic SCVs, respectively.

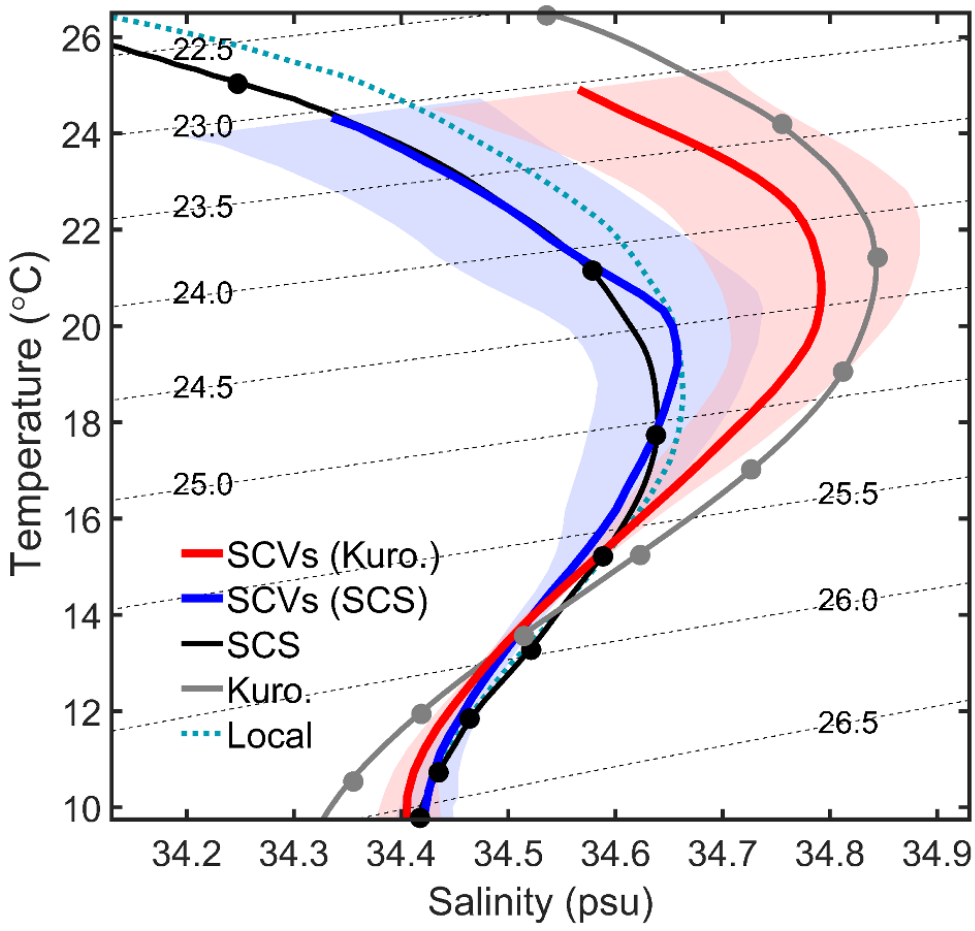

Figure 9. Mean T-S diagrams of water mass within and outside of the SCVs. Blue and red lines show the results within the SCVs that trap NESCS and Kuroshio waters, respectively. Shadings denote the standard deviations of the T/S. Black and gray lines show the results of the NESCS water and the Kuroshio water, respectively. The green dashed line shows the averaged T-S curve of local water at mooring sites. Dots on each T-S curve denote depths counted from 50 m at an interval of 50 m. Gray dashed lines show the isopycnals from 22.5 to 26.5 σ_0 at an interval of 0.5 σ_0.

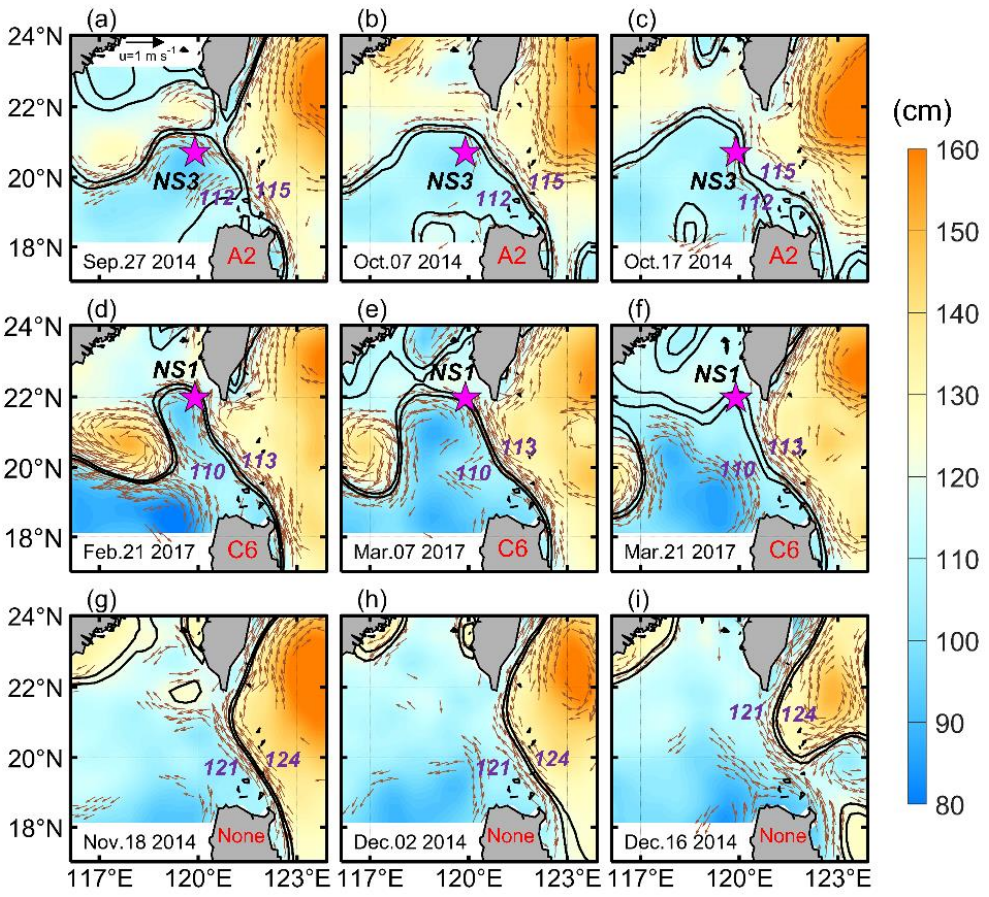

764

765 **Figure 10.** (a–c) Maps of altimeter-derived SSH and geostrophic currents in the
766 NESCS on the 20th day before, the 10th day before, and on the day the 2nd
767 anticyclonic SCV was captured by the NS3 mooring, respectively. Black lines denote
768 112 and 115 cm SSH isolines that are defined as the Kuroshio axes. The brown
769 vectors indicate surface geostrophic velocities whose magnitudes exceed 0.3 m s^{-1}.
770 Purple stars denote mooring locations that observed SCVs. (d–f) and (g–i) are the
771 same as (a–c) but for the situations where the 6th cyclonic SCV was captured by the
772 NS1 mooring and no SCVs were captured, respectively. And black lines in (d–f)
773 denote 110 and 113 cm SSH isolines, while those in (g–i) denote 121 and 124 cm
774 SSH isolines. The date of each panel is marked in the lower left corner.

775

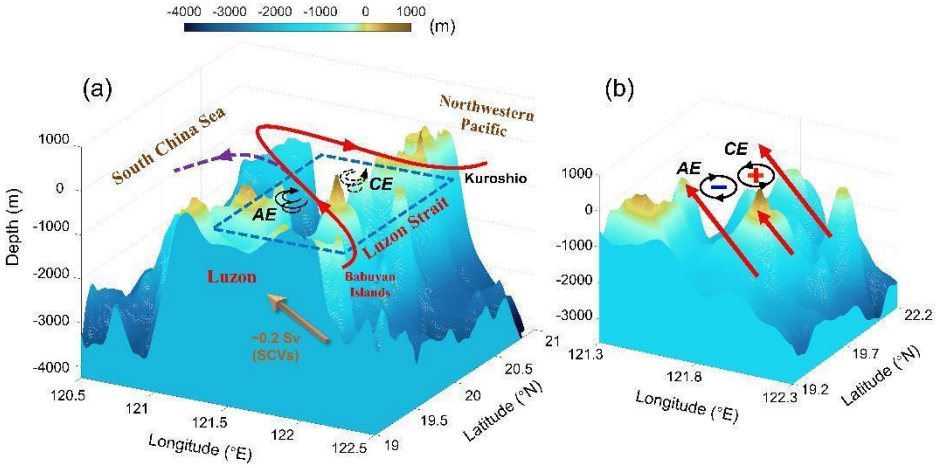

776

777 **Figure 11.** (a) The schematic diagram of generation process of Liddies through
778 Kuroshio-islands interactions. The red solid curve and the purple dashed curve
779 represent the Kuroshio intrusion including a looping path and a leaking path,
780 respectively. The black solid and dash circles represent anticyclonic and cyclonic
781 SCVs, respectively. (b) Zoom in the blue dashed square in (a), i.e., the region near the
782 Babuyan Islands. Red arrows denote the Kuroshio current near the Babuyan Islands.
783 The circles with blue negative and red positive signs represent anticyclonic and
784 cyclonic SCVs, respectively.

785